N.Gattesco, C.Amadio, C.Bedon (2015). "Experimental and numerical study on the shear behaviour of stone masonry walls strengthened with GFRP reinforced mortar coating and steel-cord reinforced repointing", Engineering Structures, 90(5): 143-157.

Experimental and numerical study of the shear behavior of stone masonry walls strengthened with GFRP reinforced mortar coating and steel-cord reinforced repointing

Natalino Gattesco[1], Claudio Amadio[2], Chiara Bedon[3]

Abstract

The research work herein presented is aimed at investigating the structural behaviour of stone masonry walls reinforced through different strengthening techniques. In particular, the difference between them is given by (i) application on both faces of a mortar coating reinforced with a GFRP (*Glass Fiber Reinforced Polymers*) mesh; (ii) application of the GFRP jacketing on one side only and (iii) application of a hybrid technique, obtained by the combination of a GFRP jacketing, on one side, and a reinforced repointing with steel-strands, on the other. Shear-compression (SC) and diagonal compression (DC) experiments were carried out on full-scale masonry walls both reinforced (RM) and unreinforced (URM), as reference. The structural effectiveness of the various reinforcing techniques is highlighted. Further assessment of test predictions was then performed by means of well-calibrated finite-element (FE) numerical models able to properly take into account the effective contribution of each specimen component. Interesting correlations were generally found between test predictions and corresponding numerical models. The experiments, as shown, generally evidenced a good effectiveness of the strengthening techniques proposed, with particular concern to that with the reinforced coating on both sides, and highlighted also the importance of the transversal connectors to prevent in plane cracks in the masonry and the detachment of the reinforced coating.

Keywords: stone masonry structures; shear strength; reinforcement techniques; GFRP jacketing; steel-cords; full-scale cyclic experiments; finite-element numerical modelling.

[1] Associate Professor. University of Trieste, Department of Engineering and Architecture, Piazzale Europa 1, 34127 Trieste, Italy.
[2] Full Professor. University of Trieste, Department of Engineering and Architecture, Piazzale Europa 1, 34127 Trieste, Italy.
[3] Ph.D., Researcher. University of Trieste, Department of Engineering and Architecture, Piazzale Europa 1, 34127 Trieste, Italy. Email: bedon@dicar.units.it.

1. Introduction

The assessment of the structural behaviour of masonry structures under seismic excitation represents a topic of interest for researchers, due to the very low tensile strength of masonry and to the large number of existing seismically inadequate masonry structures.

For this reason, various reinforcement techniques have been proposed over the last decades and investigated through experiments and numerical analyses [1].

Lin et al [2], for example, tested 25 masonry wallettes, in order to assess the strengthening capabilities of sprayed ECC (Engineered Cementitious Composite) shotcrete. In their work, the authors highlighted how the used fiber reinforced concrete can increase the ductility (up to 220%) and in-plane strength of unreinforced clay wallettes, hence resulting extremely advantageous for the seismic retrofitting of masonry structures.

Kadam et al [3] experimentally investigated the structural behaviour of reinforced masonry walls under in-plane diagonal compressive loads. In that case, the strengthening technique consisted of a Ferro-cement welded wire mesh (WWM) and micro-concrete coating.

In [4], the structural efficiency of surface mounted fiber reinforced polymer strips has been investigated. In that case, two-leaf and three-leaf walls were retrofitted by means of CFRP (Carbon Fiber Reinforced Polymers) strips. Further extended experimental investigations on clay brick masonry walls retrofitted by means of CFRP strips with various applications have been discussed also in [5, 6], where results of shake table tests have been compared for reinforced masonry specimens in terms of measured lateral strength, drift, maximum strain in composites. Quasi-static cyclic experiments on brick walls retrofitted with CFRP strips have been presented also in [7], where the effects of various anchorage systems have been emphasized. In [8], the cyclic shear-compression response of brick masonry walls with window openings, strengthened with various GFRP patterns, has been experimentally and numerically investigated. FRP retrofitted masonry walls have been tested also in [9].

Borri et al. [10] proposed a "Reticolatus" technique, consisting in small diameter, high strength stainless steel cords embedded in the repointing mortar and connected to the masonry panels by means of stainless steel connectors passing through the wall. The main advantage of this technique is that it can be applied also to masonry walls with uneven surfaces and composed of irregular components, such as historic masonry walls obtained by assembling together rubble stone elements.

In [11], the structural behaviour of multi-leaf stone masonry panels strengthened with grout injections have been investigated by means of experiments performed on 1:1 and 2:3 scaled specimens under in-plane cyclic lateral loads and simultaneous vertical compressive loads. In that experimental campaign, the effects of different levels of compression have also been investigated. Milosevic et al [12] assessed the in-plane shear strength of rubble stone masonry walls through diagonal compression experiments. The authors did not investigate the structural behaviour of reinforced specimens, mainly focusing on the behaviour of unreinforced masonry walls in order to provide useful mechanical correlations with existing works of literature. Gattesco et al. [13][14] carried out numerous diagonal compression tests on different types of masonry walls strengthened by applying on both the surfaces a mortar coating reinforced with a GFRP (Glass Fiber Reinforced Polymer) mesh. The role of the materials' mechanical properties was also investigated, and the obtained test results evidenced good effectiveness of the investigated technique. In it, the interaction between the GFRM (*Glass Fiber Reinforced Mortar*) jacketing and the masonry walls is provided by appropriate GFRP connectors. Borri et al [15] recently performed a wide series of cyclic diagonal compression experiments on masonry specimens reinforced by means of various strengthening techniques: GFRM jacketing on both the faces, "Reticolatus" system on both the faces and a combined system with GFRM jacketing on one side and "Reticolatus" on the other. All these techniques evidenced interesting effectiveness in terms of increase of shear resistance for masonry.

In this paper, the structural efficiency of GFRM jacketing and hybrid (GFRM jacketing + "Reticolatus") strengthening techniques, applied on stone masonry walls, are assessed through shear-compression (SC) cyclic experiments and diagonal compression (DC) tests. Full-scale experiments are performed on a total number of seven specimens. Further assessment and validation of experiments is then performed by means of well-calibrated, geometrically simplified but computational efficient finite-element (FE) numerical models (ABAQUS/Standard [16]). A general good agreement is found between test predictions and the corresponding numerical simulations. Although the discussed findings should be further validated by an extended experimental campaign, in conclusion, the high potentiality of the proposed techniques - as well as the effects of their main influencing parameters - are emphasized throughout the paper.

2. Experimental investigation

Two series of shear-compression (SC) experiments and diagonal compression (DC) tests were carried out on masonry specimens characterized by different strengthening approaches.

Careful attention was paid, during the experimental campaign, for the assessment of the structural effectiveness and potentiality of various solutions.

2.1. Strengthening techniques

2.1.1 GFRM jacketing technique

Experiments were firstly performed on stone masonry specimens strengthened with a special coating, composed of mortar reinforced with a GFRP mesh. The reinforced mortar coating is 30mm thick and is applied to the interested masonry surfaces as a plaster.

The main properties of the GFRM jacketing technique is that the conventional mortar reinforcement composed of steel bars is replaced by a reinforcing mesh made with GFRP wires. In this experimental campaign, specifically, the GFRP mesh consisted of AR (Alkali-Resistant)-glass fibers and epoxy vinyl ester resin (Fig.1a). Compared to traditional steel reinforcements and metal meshes, the main advantages of GFRP strengthening systems are given by their low weight, easiness of application, lack of corrosion phenomena and high electromagnetic transparency.

GFRP nets have a typical square shaped mesh, as also discussed in [14][15]. A 66×66mm^2 regular pattern was used in this work, with a cross section of the single wire equal to A_{net}= 10mm^2, obtained by assembling a set of fibers with a nominal dimension of 19-24μm. The adopted GFRP mesh (mesh density 500gr/m^2), in accordance with the technical data provided by the producer and preliminary tensile tests performed on ten small GFRP mesh specimens, can offer an average Young's modulus close to E_{bar}= 27GPa, a characteristic ultimate tensile resistance $F_{ub,bar}$= 5.7kN and an ultimate tensile strain $\varepsilon_{u,bar}$= 3%.

The structural interaction between the masonry wall and the GFRM jacketing is then guaranteed by appropriate connectors, having a typical "L" shape, composed of GFRP (Fig.1b) and generally used in a number of 6 elements per m^2.

The cross section of these connectors - obtained by assembling together a set of glass fibers (60% minimum percentage, compared to the total cross-section area of the connector) with size 19-24 μm - has a rectangular shape of nominal dimensions s_1= 12mm × s_2= 8mm. The L_1, L_2 dimensions of the L-shaped connectors used in this experimental campaign were 300mm and 100mm, respectively. Based on recommendations of the producer and three tensile tests carried out on L-shaped specimens, the adopted connectors can offer an ultimate tensile characteristic strength $F_{ub,conn}$ up to 39kN, corresponding to a tensile characteristic stress $\sigma_{ub,conn}$= 455MPa (standard deviation ±11MPa), and an average Young's modulus E_{conn}= 20.5GPa.

The L-shaped connectors are generally located in the masonry wall through ϕ= 25mm diameter passing-through holes and are superposed at least 210mm to lap splice. The structural interaction between the connectors and the masonry wall is then offered by injection of thixotropic resins. At the interception between each L-connector and the GFRP mesh, being the nodal connection of crucial importance for the effectiveness of the strengthening technique, a further 33×33mm^2 piece of GFRP mesh is then applied (Fig.1c), in order to offer a proper distribution to possible peaks of stress.

The GFRM jacketing has to be applied on both faces of the interested masonry wall. In some cases, the application of the mortar coating is possible only on one side of the masonry, because on the other side frescos or fair-face are present. In this paper, the structural efficiency of both solutions is properly assessed.

2.1.2. Hybrid "Reticolatus" technique

A hybrid solution was also investigated during the same investigative campaign. In this case, the technique consists in strengthening the masonry walls by means of a combined "Reticolatus" system and a GFRM jacketing. The "Reticolatus" technique is described in [15], where it has been applied to a large number of stone and brick masonry specimens.

The technique consists of inserting in the mortar of the repointing (generally every three joints) a continuous mesh made of AISI 316 stainless steel cords (3mm diameter). The cords are arranged in the vertical and horizontal directions, to form a net whose size typically depends on the dimensions of the stone elements. The intercepting nodes of these cords are then rigidly connected to the opposite face of the masonry wall by means of transverse stainless steel bars (typically in a number of 5 elements per m^2), able to provide a full

interaction between the cords and the specimen (Fig.2). Prior to the assembling of full-scale masonry specimens, experiments have been performed on small cord specimens, in order to assess their mechanical properties. Tensile test were performed on 10 samples and generally provided almost stable results, that is tensile failure load $F_{t,steel}$= 6.11 kN (standard deviation ±0.068kN), ultimate tensile stress $f_{t,steel}$= 1458MPa (±16.22MPa) and Young modulus E_{steel}= 81.5GPa (±15.6GPa).

The transverse threaded stainless connectors have a typical diameter of 8mm and are characterized by the presence of a ring at one of their ends. The connectors are inserted throughout the total thickness of the masonry wall (e.g. Fig.2). The metal cords constituting the reinforcing net are then passed through the rings and by partial tightening of a nut it is possible to slightly prestress them, improving their reinforcement and confinement effect.

2.2. Description of specimens

A total number of seven full-scale tests were performed throughout the experimental campaign.

Both shear-compression (SC) and diagonal-compression (DC) tests were carried-out on several double leaf masonry specimens having specific geometrical properties and reinforcement techniques. In order to assess the structural efficiency of each proposed solution, specifically, SC and DC tests were performed also on unreinforced specimens (URM). All specimens were made with rubble limestone blocks (dimensions of blocks quite variable but with an average size 150×230×90mm^3, see Figs.4, 6 and 7). The nominal dimensions of specimens were 1.50×2.00×0.35m^3 for SC tests, and 1.16×1.16x0.40m^3 for DC tests (Fig. 3).

Some experimental compression tests performed on 500×400×1000mm masonry samples provided average values for Young's modulus, compressive strength and density respectively equal to $E_{masonry}$= 2430MPa, $f_{c,masonry}$= 4.5MPa and $\rho_{masonry}$= 2100kg/m^3 [13]. The masonry walls were built by using an hydraulic lime mortar (320kg/m^3 of hydraulic lime per m^3 of mortar) with an average compressive strength – based on a total number of six preliminary experiments performed on small 100mm diameter and 200mm height cylindrical specimens – equal to $f_{c,mortar}$= 7.5MPa.

After testing the reference URM specimen (MSR1), three SC experiments were performed on further specimens characterized by the application of the above described strengthening techniques. As specified in Table 1, the structural capabilities of the URM specimen (MSR1) were compared with the experimental

results obtained on specimens reinforced with the application of a double GFRM jacketing (MSR2), a single GFRM jacketing (MSR3) and a hybrid strengthening technique (MSR4). For all the RM specimens, a total number of 24 equally spaced GFRP connectors were used (with ≈0.4m the grid size, Fig.3a). The GFRM jacketing and the "Reticolatus" techniques were then applied as described in Section 2.1.2.

The GFRM jacketing for all the RM specimens was realized by means of a lime-cement mortar. Six compressive experiments performed on small cylindrical samples provided an average compressive strength $f_{c,mortar}$= 19.2MPa. Also in the case of DC tests, the structural behaviour of an URM specimen (DC1) was compared with the test predictions obtained from specimens reinforced with a double GFRM jacketing (specimen DC2) or a hybrid technique (specimen DC3). Based on the nominal dimensions of each specimen, six GFRP connectors were equally spaced through a regular mesh pattern (with ≈ 0.4m the grid size, Fig.3b), in order to properly connect the masonry walls with the GFRP mortar coatings.

2.3. Test methods and procedures

2.3.1. Shear-compression (SC) tests

The test setup of SC experiments is illustrated in Fig.4. Each masonry specimen was laid over a reinforced concrete (RC) base having total dimensions 1.50×0.25×0.40m^3. A second equal RC element was also placed on the top of the masonry specimens, and effectively connected to a stiff steel beam able to apply both vertical and horizontal forces to the tested masonry walls (Fig.4a).

Shear-compression experiments were performed on specimens by applying first a vertical force equal to 480kN - corresponding to an average compressive pressure σ_0≈ 0.9MPa in the masonry wall - by means of two vertical electro-mechanical actuators connected to the top steel beam and to the stiff concrete floor of the laboratory, respectively (Figs.4a-4b). A third electro-mechanical actuator was used to apply horizontal forces at the top of the specimens.

19 potentiometer displacement transducers were used to survey some displacements of each specimen (Fig.4b). In particular, T1/T3 and T2/T4 transducers measured the diagonal variation on both specimen faces; T5/T7 and T6/T8 instruments surveyed the vertical deformation of the specimen at right and left vertical edges; T9 and T10 transducers measured the uplift of the specimen at the bottom edge, while T11 and T12 transducers measured the uplift of the stiff steel beam at the top of the specimen. T13 and T14

instruments were used to monitor the distance of the steel beam from the floor; at the same time, T15 and T16 transducers surveyed the masonry-concrete slip at the top and bottom edges of the specimen, respectively; T17 measured the slip of the bottom concrete element with respect to the floor; while T18 and T19 the horizontal displacement at the top of the specimen. Some details concerning the transducers application are illustrated in Figs.4c-4d. Three load cells were also used to register the vertical load at both the extremities of the wall, and the imposed horizontal shear load.

The vertical load was firstly applied, and maintained constant up to failure. Then the horizontal actuator was varied cyclically with complete inversion, by taking into account a displacement-controlled test protocol. The experiment was governed through a computer arranged with a special software to control the three actuators, so that the same total vertical load and the same vertical displacements on transducers T13 and T14 could be guaranteed during the entire test.

The horizontal top displacement was varied cyclically between two opposite values, and increasing gradually these values at the end of each cycle. The typical horizontal displacement variation sequence is summarized in Fig.5 (RM specimen MSR2). The test was stopped just before the collapse of the specimen.

2.3.2. Diagonal compression tests

To carry out DC tests, an appropriate experimental apparatus was designed to allow the application of the diagonal load without moving the specimen. The typical DC specimen, in fact, was built on a steel bench and after curing, part of the bench was removed to allow placing the steel device for applying the load at one of the bottom corners of the specimen (Fig.6a). The device has an angle welded to a robust H-shape profile and stiffened with a series of ribs, to avoid deformation of the angle. A second similar device was applied at the opposite corner of the specimen. Finally, a third device was connected to the bottom device through four steel bars, in order to provide a diagonal force by means of a hydraulic jack interposed between the top devices (Figs.6a-6b). During the experiments, as shown in Fig.6b, two couples of potentiometer transducers (T1/T3, T2/T4) were used to measure the variation of the relative distance, on both the wall surfaces, between two reference points on the diagonals (reference distance 1200mm).

The hydraulic jack was activated with a hand pump and the applied force was measured with a pressure transducer. All the transducers were connected to an electronic acquisition unit interfaced with a computer.

A sequence of loading-unloading cycles was carried out assuming load increments of 20kN at each cycle up to reaching 80% of the maximum load. Then the test was prosecuted assuming displacements increments of 0.25mm. All the experiments were stopped at the failure of specimens, or at least at the attainment of a maximum displacement of the compressed diagonal equal to 20mm.

2.4. Discussion of test results

The comparison between test results obtained from URM and RM walls generally highlighted, both for SC and DC tests, as well as for the various configurations, the high potentiality of the studied reinforcement techniques.

2.4.1. Shear-compression tests

The SC test performed on the URM specimen MSR1 manifested a typical failure mechanism characterized by the progressive opening and propagation of in-plane vertical cracks at the top of the masonry wall – due to the separation of the two masonry leaves deriving from the applied compression in the diagonal strut – and almost diagonal cracks in among the faces of the specimen, thus leading to a subsequent collapse.

In this hypothesis, specimen MSR1 reached a maximum shear load H_{max}= 155kN, a maximum lateral displacement at its top end equal to u_{max}= 11.9mm≈ 0.006*h*, being *h* the nominal height of the specimen. The conventional ultimate lateral displacement u_u, corresponding at a post-cracked residual resistance equal to 80% its maximum load carrying capacity H_{max}. Is equal to 7.9mm≈ 0.004*h*. These values are summarized in Table 2. Fig.7a presents the shear load *H*-maximum lateral displacement *u* cyclic behaviour observed during the test, while in Figs.7b-7c it is possible to notice the final crack pattern in the specimen.

Three SC tests were also performed on RM specimens MSR2, MSR3 and MSR4. All the strengthening techniques manifested a marked increase of resistance and ductility in the tested specimens, compared to the URM wall MSR1. Load *H*-lateral top displacement *u* curves obtained separately for the various RM specimens, are compared to MSR1 results in Figs.8a, 8b and 8c respectively. For them, the failure configurations are also proposed, in order to emphasize their typical collapse mechanism.

All the specimens manifested a stable cyclic behaviour, also after occurring of damage in the stone masonry wall (Figs.7-8). The exception was represented by specimen MSR3, where the application of the GFRM

246 jacketing on one side only caused parasitic out-of-plane bending in the specimen, due to the eccentricity of
247 its resisting plane with respect to the mid plane of the masonry wall. The consequent occurrence of
248 premature damage in the unreinforced surface of the specimen did not allow to carry-out a full cyclic
249 experiment (Fig.8b).
250 The experiments highlighted that the critical component of the investigated structural system is generally
251 represented by the connectors. The RM walls, although more resistant and ductile than the URM specimen,
252 failed due to the progressive collapse of some connectors (e.g. the GFRP connectors located along the
253 compressed diagonal of the masonry wall), thus due to the progressive detachment of the mortar coatings
254 from the masonry surfaces. Nevertheless, an appreciable structural efficiency was noticed.
255 Comparative calculations are proposed also in Table 2 for all the SC experiments. In it, R_{load} represents the
256 ratio of the maximum attained shear load for each RM specimen, compared to the predicted strength of the
257 URM specimen MSR1. Similarly, the R_{disp} ratio is representative of the relationship between the failure
258 lateral displacements u_u attained by the various RM walls, compared to the failure deformation of specimen
259 MSR1. In the same Table, the values of maximum load H_{max}, maximum lateral displacement u_{max}, ultimate
260 lateral displacement u_u and the corresponding drift u_u/h are also collected. In it, finally, the experimental
261 equivalent tensile strength f_t values are also directly calculated as:

262 $$H_{\max} = Bt\frac{f_t}{\beta_{shear}}\sqrt{1+\frac{\sigma_0}{f_t}}, \qquad (1)$$

263 being Eq.(1) suitable for the estimation of the shear failure strength of stone masonry walls [17]. In Eq.(1), in
264 particular, B and t respectively denote the width and thickness of the tested specimens, σ_0 is representative
265 of the average compressive stress in specimens due to the applied compressive vertical loads and β_{shear} is the
266 shear distribution factor, assumed equal to 1.5 for the tested specimens, based on their height to width ratio.
267 In this hypothesis, the last right column of Table 2 proposes the ratio R_t between the equivalent tensile
268 strength of RM specimens, compared to that of URM one.
269 Based on test results collected in Table 2, it can be seen that independently on the typology of reinforcement,
270 the ductility of the tested specimens increased up to two times, compared to specimen MSR1. Also in terms
271 of total strength, appreciable contributions offered by the various techniques were found, with increments of

total resistance comprised between a minimum ratio 1.17 for the specimen MSR3 with a single GFRM coating and a maximum ratio 1.39 for the specimen MSR2 with a double GFRM coating. A greater increment in terms of equivalent tensile resistance was found in RM specimens with respect to the URM one. As expected, the maximum strengthening contribution was offered by the double GFRM jacketing (specimen MSR2). The specimen MSR3 reinforced with a single GFRM coating resulted less effective, since due to the application of only one reinforced jacket the confining effect was almost negligible and the in-plane response of the wall was eccentric with respect to its middle plane. However, a ductility increase comparable to that of the other strengthened specimens was obtained.

The third reinforcing technique (MSR4, hybrid system) offered an increment in resistance and ductility almost comparable to the double GFRM coating. In this sense, the test confirmed that the presence of reinforcement on both the faces of specimens can be extremely efficient, since it allows to avoid a premature disaggregation of the stones, as well as to provide a stable confining effect, hence avoiding the opening and progressive propagation of compressive cracks (e.g. specimen MSR1).

In any case, it should be noticed that the failure of connectors occurred in all tested specimens, causing the premature detachment of the reinforced coating and consequently a reduced effectiveness of the strengthening techniques (Fig.8).

2.4.2. Diagonal compression tests

DC experiments confirmed the high strengthening capabilities of the investigated reinforcement techniques. Compared to SC experiments, the reinforced DC specimens manifested larger increment of resistance and ductility for the tested masonry walls. This effect was mainly due by a full interaction - up to failure - between the GFRM jacketing or hybrid reinforcement and the corresponding masonry walls. While SC reinforced specimens emphasized a mainly local failure mechanism in few connectors, leading to a progressive detachment of the almost undamaged mortar coatings from the specimen surfaces, DC tests - due to a different loading configuration - did not manifest local failure mechanisms in the connectors.

In Fig.9, for example, graphs of the applied compressive force C against the diagonal compressive strain ε_c obtained for the specimens DC1, DC2 and DC3 are proposed. All the curves (skeleton curves derived from cyclic loading-unloading test measurements) are extended up to a compressive deformation ε_c equal to 0.006. These plots generally highlight a significant increase of the maximum resistance in both the RM specimens, but manifest a considerably higher value of resistance especially for the specimen strengthened with reinforced mortar jacket (DC2).

During tests, all the specimens showed a stop in the resistance increase at the occurrence of first cracks. In the case of the RM specimens, the maximum attainted load C_{max} remained almost constant up to a diagonal compressive deformation equal to 0.003, and started to reduce slightly for larger deformations only. In the URM specimen DC1, in contrary, after first cracking (Fig.10), the propagation of cracks caused a progressive reduction of resistance.

The specimen DC2, strengthened with GFRP reinforced mortar coating on both faces, evidenced the occurrence of many parallel cracks after the first one (Fig.11). In the hybrid strengthened specimen DC3, in contrary, a slight out of plane deflection due to asymmetric strengthening (e.g. GFRP reinforced mortar coating stiffer than the reinforced repointing) anticipated the occurrence of diagonal cracks in the masonry wall and the failure propagation of mortar joints, through the wall thickness, although the reinforced coating remained almost uncracked up to failure. Due to the progressive damage of the masonry specimen (Fig.12), the applied load did not increase further (Fig.9).

Further comparative calculations are collected in Table 3, in the form of maximum load C_{max}, shear strain at the onset of cracking γ_{cr} and shear deformation γ_u corresponding to a 20% reduction of the maximum load C_{max} in the post-cracked phase. Both the shear deformations γ_{cr} and γ_u were estimated as the sum of the absolute measured diagonal strains $\gamma = |\varepsilon_t| + |\varepsilon_c|$, with the subscripts t and c refer to diagonals in tension and compression respectively.

In the same table, the ratio R_{load} between the maximum loads of RM and URM specimens, the ratio R_{strain} between the shear strain γ_u at 20% reduction of the load after the peak value and the shear strain at the onset of cracking γ_{cr} are also reported. The first ratio (R_{load}) evidences the increase in resistance with respect to URM specimen, while the second (R_{strain}) emphasizes the ductility of specimens.

As shown, the resistance of the specimen strengthened with GFRM jacketing on both faces (DC2) resulted almost quadruple that of the unstrengthened specimen DC1, whereas the resistance of the specimen reinforced with the hybrid system (DC3) was 70% higher than that of URM specimen.

In terms of ductility (R_{strain}), DC experiments performed on both the RM samples confirmed the high capabilities of the studied techniques. R_{strain} ratios obtained for DC2 and DC3 specimens manifested in fact a 20% increase and 100% increase respectively of ductility, compared to the URM specimen DC1.

The higher resistance of the specimen strengthened with the reinforced coating applied on both faces (DC2), with respect to that reinforced with the hybrid system, was mainly due to both the presence of two reinforced layers and the symmetry of the applied strengthening technique, with respect to the mean plane of the specimen. On the contrary, the load carrying behaviour up to failure of the specimen reinforced with the hybrid system (DC3) was partly affected by a parasitic out of plane flexural mechanism (Fig.12b). This failure mechanism resulted in slight improvement of resistance capacities, although high ductility was noticed.

In Table 3, the values of the equivalent tensile strength f_t for the URM and RM of DC tests are also proposed. The equivalent tensile strength f_t was calculated, in accordance with RILEM recommendations [18], using the relationship:

$$f_t = \alpha \frac{C_{\max}}{A_w}, \qquad (2)$$

being α= 0.5, C_{max} the maximum compressive load and A_w the cross-sectional area of the tested specimens.

Although DC experiments were carried out on three specimens only, the obtained results generally provided close agreement with earlier experimental studies (e.g. [14]), where the structural effectiveness of the same reinforcement techniques has been assessed by means of DC tests performed on four types of masonry walls. The current DC and SC tests, consequently, can represent a further experimental background for further optimizations.

3. Finite-element numerical interpretation of experiments

Assessment of full-scale experiments was then carried out by means of opportunely calibrated finite-element (FE) numerical models [16]. Comparisons are presented in this paper for the URM (MSR1) and RM (MSR2,

351 double GFRM coating; MSR3, single GFRM coating) SC specimens (Section 3.1), as well as for the URM
352 (DC1) and RM (DC2, double GFRM jacketing) specimens (Section 3.2).
353
354 **3.1. Shear-compression experiments**
355 **3.1.1. Unreinforced specimen FE-MSR1**
356 In accordance with the test setup presented in Section 2.3, the model FE-MSR1 consisted of two concrete
357 elements, a masonry wall and a steel contrast beam.
358 Both the concrete and the masonry elements were described in the form of 3D solid, 8-node brick elements
359 available in the ABAQUS/Standard element library (C3D8R type). In order to save the computational cost of
360 simulations, a regular mesh pattern with a constant mesh size of l_{mesh}= 0.08m was used. The structural
361 interaction between masonry and the concrete components, having coinciding mesh nodes between the
362 contact surfaces, was then guaranteed by means of rigid connections (surface-to-surface "*tie*" constraints
363 [16]) able to prevent possible relative displacements and rotations between the interested nodes (Fig.13a).
364 The upper stiff steel element (Fig.4) was described in the form of shell elements, lying on a *x*-*z* plane and
365 having a regular mesh pattern composed of 4-node elements (l_{mesh}= 0.08m). Possible relative displacements
366 between these coinciding steel-masonry nodes were again avoided by means of a "*tie*" constraint (Fig.13a).
367 The model FE-MSR1 was then rigidly restrained at the base (u_x= u_y= u_z= 0, Fig.13b).
368 The typical simulation consisted in a static incremental, geometrical nonlinear, displacement-controlled
369 analysis divided in two steps. In the first step, the vertical pre-compression was applied in the form of a
370 vertical, uniformly distributed pressure *q* applied to the upper surface of the stiff steel beam. Gravity loads of
371 concrete, masonry and steel components were also taken into account. The second step was carried-out on
372 the pre-compressed FE-model, and a monotonic history of horizontal, linear rising lateral displacements u_x
373 was imposed to the end nodes of the top concrete element (Fig.13b).
374 Careful consideration was paid for the mechanical characterization of materials. Concrete, representative of
375 the top and bottom RC elements, was assumed as an indefinitely elastic and isotropic material (E_{cls}= 40GPa,
376 ν_{cls}= 0.20 and ρ_{cls}= 2500kg/m^3). For steel, an indefinitely linear elastic, isotropic material was also defined
377 (E_{steel}= 201GPa, ν_{steel}= 0.25 and ρ_{steel}= 7850kg/m^3). Finally, masonry was described in the form of an

equivalent, homogeneous and isotropic material having a linear elastic behaviour up to failure ($E_{masonry}$= 2430MPa, $\nu_{masonry}$= 0.15 and $\rho_{masnory}$= 2100kg/m^3), while its post-cracked behaviour was then based on an appropriate calibration of the "*concrete damaged plasticity*" (CDP) mechanical model [16].

This mechanical model, developed by Lubliner et al. [19] for RC components and further elaborated by Lee and Fenves [20], well applies to materials with quasi-brittle behaviour such as masonry. Recent examples for masonry structural systems can be found in [21][22]. In the CDP model, the yield surface function takes the form of an extended Drucker-Prager classical model and is based on the proposal of Lubliner et al. [19], successively modified in accordance with [20] to take into account different evolution of strength under tensile and compressive stresses [16].

Nevertheless, its main input parameters must be properly assessed. The inelastic compressive and tensile behaviours are in fact described in the form of a multi-hardening plasticity and a scalar isotropic damaged elasticity characteristic curves (Fig.14). In this work, the main input parameters were defined in accordance with [23]. The dilation angle Ψ and the ratio f_{b0}/f_{c0} between the equibiaxial compressive failure stress to the uniaxial compressive one, specifically, were assumed equal to 48° and 1.16 respectively, while visco-plastic phenomena were neglected. Tension stiffening effects were described in the form of a stress-strain post-failure relationship (Fig.14a and Table 4), including also damage evolution and propagation. For the post-cracked compressive behaviour, similarly, possible crushing phenomena were taken into account by means of the constitutive stress-strain parameters proposed in Fig.14b and Table 4 respectively.

3.1.2. Reinforced specimen FE-MSR2 (double GFRM jacketing)

A second FE-model was developed for the reinforced specimen MSR2. In it, the URM specimen (Section 3.1.1) was properly modified, by introduction of the GFRP connectors and two mortar coatings.

The mortar coatings were described in the form of shell elements, lying on two *x*-*y* planes and having a rectangular, uniform cross-section of total thickness $t_{coating}$= 30mm. In it, the reinforcing GFRP bars were also taken into account, by means of two orthogonal GFRP layers having the nominal geometrical properties of the actual GFRP net (Section 2.1.1). A regular, 4-node element mesh pattern was then used for the

geometrical description of these shell elements, so that the mesh nodes could coincide with the mesh nodes of the adjacent masonry wall, on both the specimen faces.

An appropriate surface-to-surface interaction was then assigned to the masonry and mortar coating surfaces in contact (Fig.15a). The full-scale experiment MSR2 (Section 2.4.1) highlighted in fact – especially in the initial loading phase and prior to the failure of some L-connectors – an almost full interaction between the masonry panel and the mortar jacketing against the applied shear loads, thus a coupled in-plane behaviour of the RM specimen, due to the roughness of the masonry and jacketing surfaces in contact. In the direction perpendicular to the plane of the wall, conversely, the interaction between masonry and jacketings was primarily given by the L-connectors only, hence resulting affected by local peaks of axial tensile loads. In this sense, the MSR2 FE-model was properly implemented so that the interaction between the specimen components was correctly reproduced. The possible sliding of the mortar coating on the masonry surface was described by means of a static friction coefficient $\mu = 0.8$ (comparable with $\mu = 0.7$ for masonry-to-masonry and $\mu = 0.8$ for concrete-to-concrete interactions). This value was assumed in order to take into account the lack of roughness in the shell-to-solid contact surfaces, so that no relative sliding was prevented prior to the collapse of the GFRP connectors. In the direction perpendicular to the contact surfaces, possible detachments of the GFRM jacketing from the masonry faces were neglected. For the same reason, based on the observation of experimental failure mechanisms, the possible occurrence of damage was accounted in the mechanical description of the GFRP connectors, as discussed in the following paragraphs.

The L-shaped GFRP connectors were in fact simplified in the form of linear beam elements (Fig.15b), having the same nominal $s_1 \times s_2$ cross-section of the actual connectors (Fig.1). The structural interaction between each connector and the external mortar coatings was guaranteed by "*join*" connectors able to avoid possible relative displacements between the linked nodes. At the same time, the possible local failure at the connection between the masonry wall and the mortar coatings (e.g. collapse of the GFRP connectors highlighted by full-scale SC tests) was taken into account by means of an appropriate mechanical calibration of the GFRP fibers constituting the L-connectors.

Careful consideration was in fact dedicated to the mechanical characterization of the mortar coating, the GFRP bars and the GFRP connectors respectively. In the first case, the CDP mechanical model was

calibrated to reproduce the effective mechanical properties of the adopted hydraulic mortar (Section 2.2), with $E_{jacketing}$= 20GPa, $\nu_{jacketing}$= 0.2, $\rho_{jacketing}$= 2100kg/m^3. For the GFRP bars, an isotropic, elasto-plastic mechanical behaviour was taken into account, with E_{bar}=27GPa, ν_{bar}= 0.3, ρ_{bar}=2400kg/m^3 and $F_{ub,bar}$= 5.7kN the ultimate tensile strength (Section 2.1). For the GFRP connectors, finally, the same elastic parameters given in Section 2.1.1 were taken into account (E_{conn}=20.5GPa, ν_{conn}= 0.3, ρ_{conn}= 2400kg/m^3). Concerning the tensile strength of the material, conversely, this value was calibrated to further extraction tests.

Four experiments, specifically, were performed on small samples consisting of a single L-shaped GFRP connector (Fig.1b) interacting with a 380×380mm^2 portion of 30mm-thick mortar jacketing (Fig.16). When assembling these small specimens, careful attention was paid for the description of the geometrical detail of the GFRP connector-to-mortar interception, so that the actual nodal connection could be correctly reproduced (Fig.16). A 33×33mm^2 piece of GFRP mesh was also introduced in the small specimens. As a result, the shortest edge of each GFRP connector (L_2, Fig.1b) was embedded in the mortar coating together with the GFRP mesh, whereas the other connector edge (L_1, Fig.1b) was kept free. Once rigidly fixed the base surface of mortar coating over a flat support, the typical extraction experiment consisted in applying a quasi-static, monotonic tensile axial load at the free end of each GFRP-connector (L_1 edge), up to failure. All these small specimens manifested almost a stable behaviour, characterized by a linear elastic mechanical response up to the occurring of first damage mechanisms. Failure occurred due to cracking and fragmentation of the mortar coating – close to the GFRP connector – with progressive sliding and subsequent extraction of the GFRP connector itself. An average failure tensile load $F_{ub,conn}^*$ = 5.7kN (standard deviation ± 0.72kN) and yielding stress $\sigma_{ub,conn}^*$ = 58MPa were obtained from these extraction experiments (e.g.≈ 1/7 the tensile strength of the L-shaped connectors (Section 2.1.1)). In accordance with the damage mechanisms observed in the SC full-scale experiments (e.g. detachment of mortar coatings from the faces of the masonry wall, Section 2.4) and these further test results – due to the lack in the presented FE-models of possible detachments at the GFRP connector-to-mortar coating interface – the average extraction failure tensile load $F_{ub,conn}^*$ was considered well representative, although in a simplified way, of possible local collapse

phenomena in the typical GFRP connector-to-jacketing interceptions. The so assembled FE-MSR2 model was successively restrained and loaded in the same way of the unreinforced model FE-MSR1 (Fig.13b).

3.1.3. Reinforced specimen FE-MSR3 (single GFRM jacketing)

The third FE-model was directly derived from the FE-MSR2 model.

The same material mechanical properties, loading conditions, boundaries and solving approach of the FE-MSR2 model were taken into account. In this latter case, to assess the structural efficiency of a single GFRM jacketing, a single mortar coating was described. The GFRP connectors were consequently linked by means of "*join*" connectors at the shell GFRM coating, on one specimen face, and at the corresponding mesh nodes of the masonry wall, on the opposite face.

3.1.4. Discussion of SC numerical results

Despite the simplified FE-modelling assumptions, the so obtained numerical models generally provided interesting correlations with the corresponding SC test results. Comparative examples are proposed in Fig.17 for the URM specimen MSR1, compared to specimens MSR2 (Fig.17a) and MSR3 (Fig.17b). The unreinforced FE-MSR1 model manifested the typical expected behaviour, with damage located along the diagonal of the panel (Fig.18) and limited ductility. The use of a double GFRM jacketing, otherwise, manifested in markedly increase of resistance and ductility for the same specimen. Numerical simulations confirmed the high confining capabilities of the double mortar coating, hence providing a markedly uniform distribution of stresses in the masonry panel (Fig.19a) and a more stable behaviour up to failure.

No damage was noticed in the GFRM coatings (Fig.19b), in accordance with the corresponding test results.

At the same time, the numerical simulations confirmed the fundamental role of the GFRP connectors, being of crucial importance for the full structural interaction between the GFRM jacketing and the masonry panel.

Based on a detailed analysis of numerical predictions, progressive damage was found in the connectors along the diagonal of the masonry specimen, that is where the mortar coatings offer the maximum confining contribution to the masonry wall.

The primary role of GFRP connectors consists in fact in preventing possible out-of-plane deformations of the GFRP jackets, due to progressive damage in the masonry wall. As far as the maximum tensile stresses in

each GFRP connector do not exceed their plastic strength $\sigma_{ub,conn}^{*}$, the confining contribution of the double GFRP jacketing shows a significant increase of in-plane shear strength for the specimen (Fig.17a) and almost a uniform distribution of stresses in the masonry wall (Fig.19, u_{max}= 3mm). Otherwise, once the maximum tensile stresses in the GFRP connectors exceed $\sigma_{ub,conn}^{*}$, the L-shaped connectors along the compressed diagonal are not able to carry-on additional loads. This effect leads to the attainment of higher tensile stresses in the resting GFRP connectors, as well as to a reduced confining effect of the GFRP jackets and to a partial decrease of the total in-plane shear strength for the entire specimen (Fig.17, u_{max}= 10mm).

The FE-MSR3 numerical model, although strengthened by a single mortar coating only, also provided numerical predictions rather in good agreement with the corresponding test results (Fig.17b). The predicted failure mechanism was comparable to that of the FE-MSR2 model. In Fig.17b, for example, it is interesting to notice that once the diagonal GFRP connectors fail, the mortar coating alone – although undamaged – is not able to provide appropriate confining contributions to the adjacent masonry panel. As a result, the in-plane shear load-top lateral displacement curve of the damaged FE-MSR3 model coincides with that of the damaged unreinforced FE-MSR1 model (Fig.17b, for maximum top displacements larger than ≈9mm) . Further numerical simulations were thus performed on the double reinforced FE-MSR2 model, and results proposed in Fig.17a were compared to numerical predictions obtained by the same FE-MSR2 model deprived of the GFRP connectors (e.g. masonry panel and rigidly attached mortar jacketings).

These further numerical simulations highlighted that although an idealized, full coupling against orthogonal pressures was taken into account between masonry and jacketings , the mortar coatings alone cannot provide appropriate strengthening contributions to the same specimen (Fig.20, "FE-MSR2, no GFRP connectors").

Conversely, the use of GFRP connectors with higher ultimate tensile resistance $\sigma_{ub,conn}^{*}$ typically resulted in a partial improvement of the structural efficiency provided by the double mortar coating. This effect can be seen from Fig.20, where the results of the reference FE-MSR2 model are compared with the results of further FE-MSR2 models, obtained by progressively increasing the ultimate tensile resistance $\sigma_{ub,conn}^{*}$ of the connectors. The same simulations also highlighted that – for the studied specimen – an ultimate tensile resistance up to 2.5-3 times the experimentally derived value $\sigma_{ub,conn}^{*}$ can provide a≈48% increase of the ultimate resistance predicted for the MSR2 specimen, with also an appreciable increase of ductility. As far as

the $\sigma_{ub,conn}^{*}$ further increases, however, the GFRP connectors only do not provide additional structural benefits to the specimen, and failure of the RM wall occurs due to damage propagation in the mortar coatings and in the masonry panel, rather than in the GFRP connectors, thus resulting in progressive decrease of ductility. Consequently – although the presented numerical studies still require further extended experimental validation – it is clear that all the components should be properly designed (depending on the mechanical properties of masonry) so that the structural effectiveness of the investigated strengthening techniques could be maximized.

3.2. Diagonal compression experiments

As for the SC samples, appropriate FE-numerical models were successively carried-out for the DC samples. The URM specimen (FE-DC1 model) was mechanically characterized as discussed in Section 3.1. Based on the test setup given in Section 2.3, the stone masonry wall was subjected to a monotonic history of linearly increasing diagonal compressive forces, up to failure.

The reinforced DC2 (double GFRM jacketing, FE-DC2 model) was also described in ABAQUS/Standard. In doing so, each reinforcement component (mortar, GFRP mesh and L-shaped GFRP connectors), and their structural interaction were described as discussed for the corresponding SC samples (Section 3.1).

Comparative numerical and experimental plots are proposed for DC specimens in Fig.21.

As shown, a general good agreement was found between the DC specimens and the corresponding FE-models. FE-DC numerical models confirmed the high potentiality of the studied techniques, confirming the marked confining capabilities of the GFRM jacketings compared to hybrid technique.

It is also interesting to notice, differing from SC experiments, that the DC tests and the corresponding numerical models highlighted a lower involvement in the global resisting mechanism of the L-shaped connectors, hence resulting in a markedly higher effectiveness of the same strengthening techniques. In the case of FE-DC2 model, for example, maximum tensile stresses attained in the GFRP connectors typically resulted equal to ≈1/5 the calibrated failure stress $\sigma_{ub,conn}^{*}$. Careful attention should be generally paid, in this context, to the adopted test protocol. It is clear, in fact, that discrepancies between SC and DC results

538 discussed in this paper could be partly affected – for a same strengthening technique – by the specific
539 loading condition of the tested samples.
540

541 **4. Summary and conclusions**

542 Full-scale shear compression (SC) and diagonal compression (DC) experiments were performed on seven
543 stone masonry walls in various retrofitting conditions. Compared to the structural capabilities of the
544 'reference' unreinforced specimens (URM), the efficiency of (i) a double GFRM jacketing, (ii) a single
545 GFRM jacketing and (iii) a hybrid (GFRM coating + "Reticolatus") retrofitting technique were assessed by
546 means of full-scale experiments and Finite-Element numerical simulations. Based on extended discussion of
547 test predictions and further assessment of experiments by means of properly calibrated FE-models,
548 specifically, it was shown throughout the paper that:

549 • Both the SC and the DC experiments evidence a general and significant increase of the original
550 resistance and ductility for all the tested specimens, compared to the URM one.The observed failure
551 mechanisms typically emphasized the crucial role of the GFRP connectors, for the tested specimens.
552 Especially in the case of SC experiments - due to the simultaneous action of axial loads ($\sigma_0 \approx$
553 0.9MPa) and cyclic shear forces - the reinforced (RM) specimens failed due to local collapse
554 mechanisms of few GFRP connectors, hence due to the progressive detachment of the almost
555 undamaged GFRM jacketing from the masonry surfaces, and to a subsequent disaggregation of the
556 mortar coatings from the stone elements.

557 • Further assessment of full-scale experiments was also carried out by means of Finite-Element (FE)
558 solid models able to properly reproduce the structural interaction between the various components of
559 each full-scale specimen, as well as the corresponding failure mechanisms. The FE-analyses
560 generally provided interesting correlation between numerical and experimental results, hence
561 confirming – although the limited number of full-scale experiments – the capabilities and
562 potentialities of the studied retrofitting approaches.

563 • Additional parametric FE-studies highlighted the importance of an appropriate design of the GFRP
564 connectors, compared to the mechanical properties of masonry and mortar coatings. For the tested

SC specimen with double jacketing (MSR2), for example, it was shown that an ultimate tensile resistance of the GFRP connectors at least 2.5-3 times higher than the reference value would provide a ≈48% increase of the RM specimen strength. Conversely, further increase of the ultimate resistance of the GFRP connectors would result in negligible additional benefits and a collapse mechanism governed by damage propagation in the mortar jackets.

Although further studies are required for a proper assessment and optimization of the investigated techniques (e.g. position and dimension of GFRP connectors, jacketing-to-masonry stiffness and strength ratio, etc.), in conclusion, experimental and numerical studies discussed in this paper highlighted the general structural efficiency and validity of all the examined solutions. It is thus expected that detailed discussion proposed in this work could represent a valid background for future improvements and investigations.

References

[1] Bhattacharya S, Nayak S, Dutta SK (2014). A critical review of retrofitting methods for unreinforced masonry structures. International Journal of Disaster Risk Reduction, 7: 51-67.

[2] Lin YW, Wotherspoon L, Scott A, Ingham JM (2014). In-plane strengthening of clay brick unreinforced masonry wallettes using ECC shotcrete. Engineering Structures, 66: 57-65.

[3] Kadam SB, Singh Y, Li B (2014). Strengthening of unreinforced masonry using welded wire mesh and micro-concrete – Behaviour under in-plane action. Construction and Building Materials, 54: 247-257.

[4] Dizhur D, Griffith M, Ingham J (2014). Out-of-plane strengthening of unreinforced masonry walls using near surface mounted fibre reinforced polymer strips. Engineering Structures, 59: 330-343.

[5] El Gawady MA, Lestuzzi P, Badoux M (2006). Aseismic retrofitting of unreinforced masonry walls using FRP. Composites: Part B, 37: 148-162.

[6] El Gawady, M.; Lestuzzi, P.; Badoux, M. (2005). In-Plane Seismic Response of URM Walls Upgraded with FRP. Journal of Composites for Construction; 9: 524-535.

[7] Bischof et al. 2014. On the Use of CFRP Sheets for the Seismic Retrofitting of Masonry Walls and the Influence of Mechanical Anchorage, Polymers 2014, 6, 1972-1998

[8] Kalali, A.; Kabir, M.Z (2012). Cyclic behavior of perforated masonry walls strengthened with glass fiber reinforced polymers, Scientia Iranica; 19(2), 151-165.

[9] Prota, A.; Manfredi, G.; Nardone, F. (2008). Assessment of Design Formulas for In-Plane FRP Strengthening of Masonry Walls. Journal of Composites for Construction; 12: 643-649

[10] Borri A, Corradi M, Speranzini E, Giannantoni A (2010). Reinforcement of historic masonry with high strength steel cords. Masonry Int 23(3); 79-90.

[11] Silva B, Dalla Benetta M, da Porto F, Modena C (2014). Experimental assessment of in-plane behaviour of three-leaf stone masonry walls. Construction and Building Materials, 53: 149-161.

[12] Milosevic J, Sousa Gago A, Lopes M, Bento R (2013). Experimental assessment of shear strength parameters on rubble stone masonry specimens. Construction and Building Materials, 47: 1372-1380.

[13] Gattesco N, Boem I, Dudine A (2013). Behavior of existing masonry strengthened with a GFRP reinforced mortar coating. Proceedings of the XIV International Conference on Civil, Structural and Environmental Engineering Comupting, CC2013, 3-6 September 2013, Cagliari, Italy.

[14] Gattesco N, Boem I, Dudine A (2014). Diagonal compression tests on masonry walls strengthened with a GFRP mesh reinforced mortar coating. Bulletin of Earthquake Engineering, Springer, published online (DOI 10.1007/s10518-014-9684-z).

[15] Borri A, Castori G, Corradi M, Sisti R (2014). Masonry wall panels with GFRP and steel-cord strengthening subjected to cyclic shear: An experimental study. Constriction and Building Materials 56: 63-73.

[16] ABAQUS Computer Software (v.9.12) and User's Manual. Simulia, Dassault Systemes.

[17] Turnšek V, Čačovič F. Some experimental results on the strength of brick masonry walls. In: Proceedings of the 2nd international brick masonry conference, Stoke-on-trent; 1970, p. 149–56.

[18] RILEM TC 76-LUM. Diagonal tensile strength tests of small wall specimens, 1991. In: RILEM, Recommendations for the Testing and Use of Constructions Materials. London: E& FN SPON; 1994, p. 488–89.

[19] Lubliner J, Oliver J, Oller S, Onate E (1989). A plastic-damage model for concrete. Int. J Solids Structures; 25(3): 299-326.

[20] Lee J, Fenves GL (1998). Plastic-damage model for cyclic loading of concrete structures. J Eng Mechanics; 124(8): 892-900.

[21] Pandey AK, Bisht RS (2014). Numerical Modelling of Infilled Clay Brick Masonry Under Blast Loading. Advances in Structural Engineering; 17(4): 591-606.

[22] Xiong XY, Xue RJ, Zhang S, Wang LJ (2014). The Finite Element Analysis on Seismic Performance of Ring Beam and Constructional Column with Different Storey in Masonry Building. Advanced Materials Research; Vols. 919-921, pp. 1016-1019.

[23] Gattesco N, Franceschinis R, Kristek V, Kravstov A, Rimal J (2012). Strengthening Effectiveness of Ancient Masonry Bridges. Proc. of IABMAS 2012, Stresa, Italy.

Acknowledgements

Fibre Net Srl is gratefully acknowledged for providing the test specimens. Dr. Franco Trevisan and Dr. Andrea Cernigoi (University of Trieste, Department of Engineering and Architecture) are also acknowledged for the technical support and collaboration during the experimental program.

Figure 1

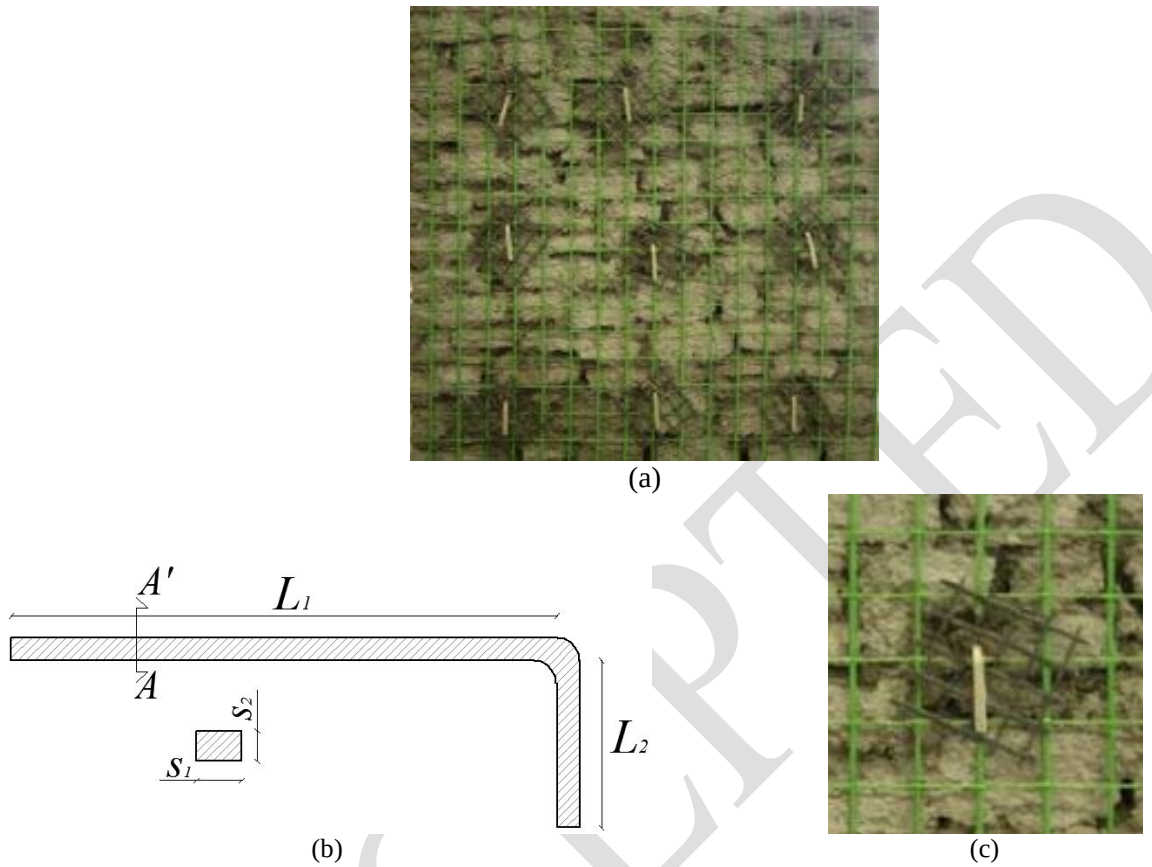

(a) (b) (c)

Fig.1. GFRM jacketing technique. (a) Example of GFRP mesh; (b) geometry and cross-section of an L-shaped connector; (c) connection detail.

Figure 2

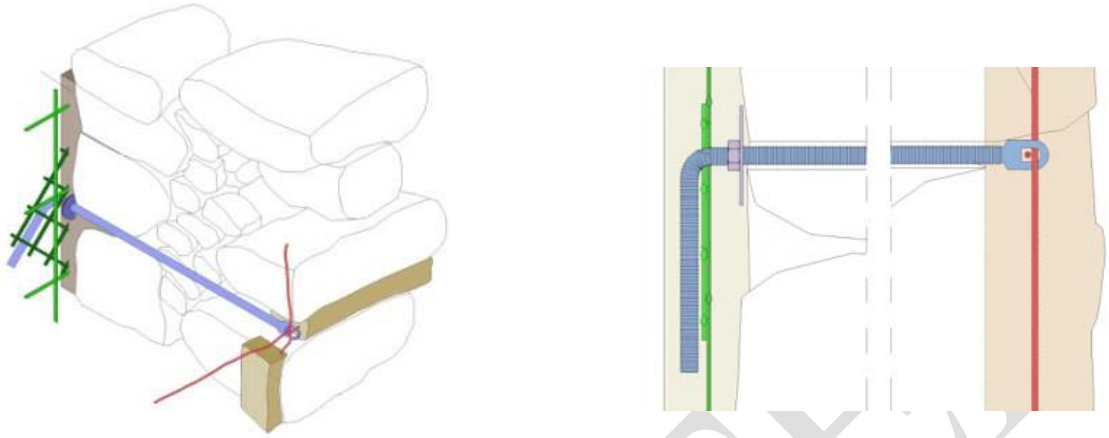

Fig.2. Hybrid "Reticolatus" strengthening technique. Details of the connector passing-through the masonry wall.

Figure 3

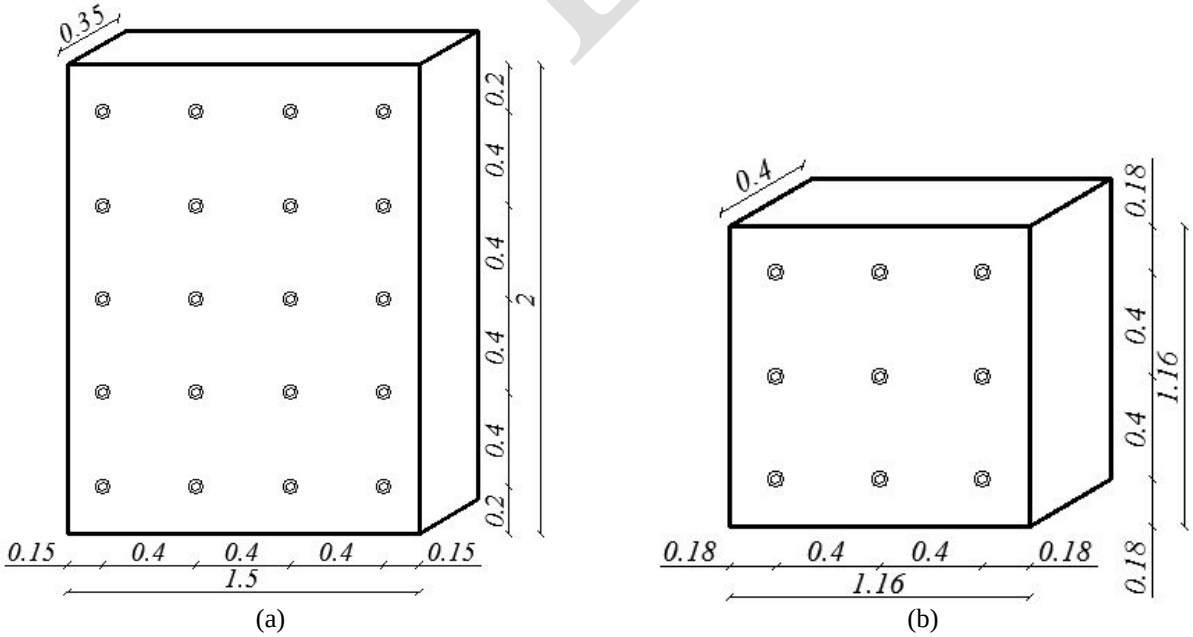

Fig.3. Position of ϕ=25mm passing-through holes for the allocation of GFRP connectors. (a) SC specimens; (b) DC specimens. Nominal dimensions in m.

660 **Figure 4**

661

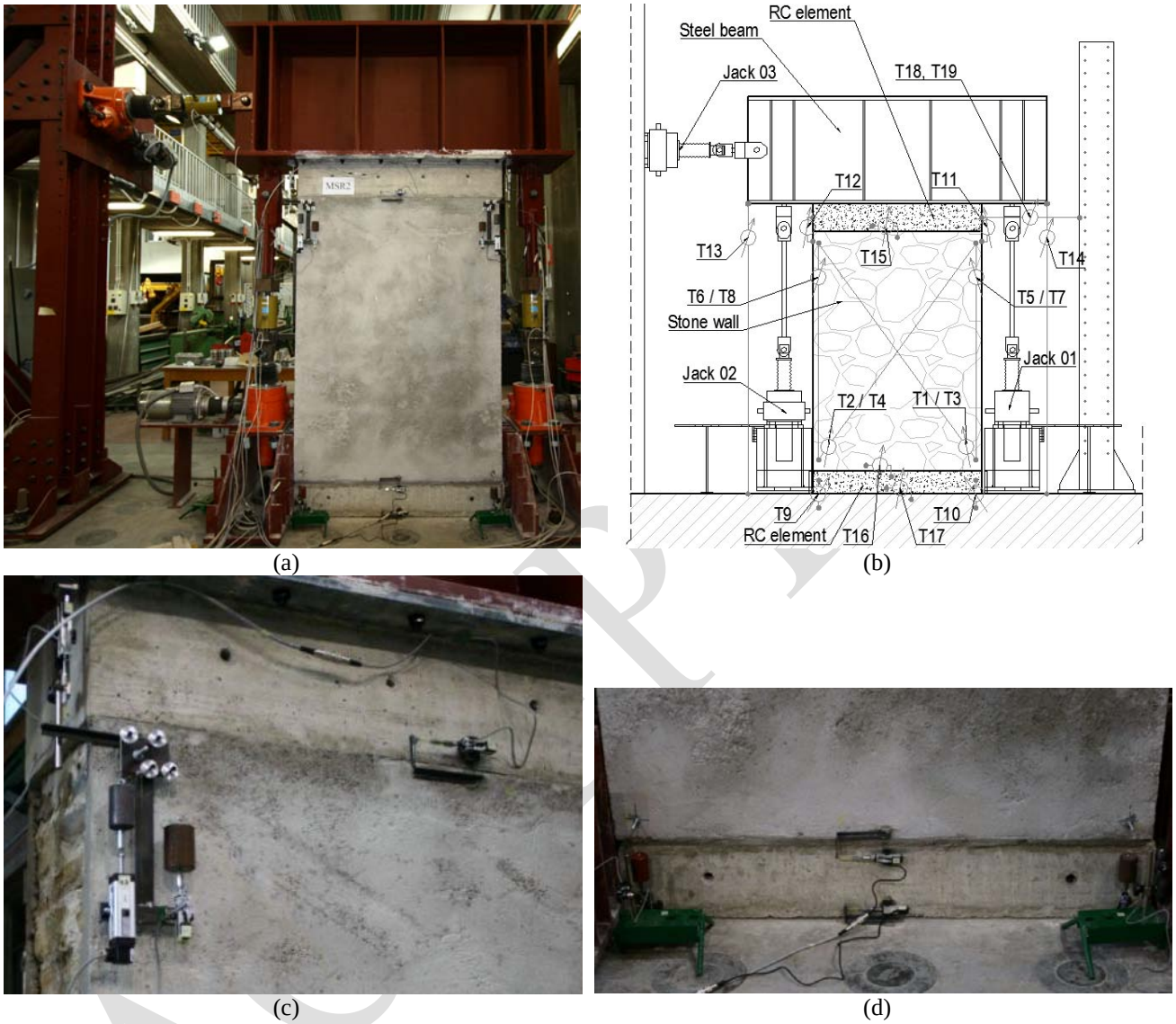

Fig.4. SC experiments. (a) Test setup; (b) position of transducers; instrumentation details (c) at the top and (d) at the base of the specimen.

662

663

664 # Figure 5

665

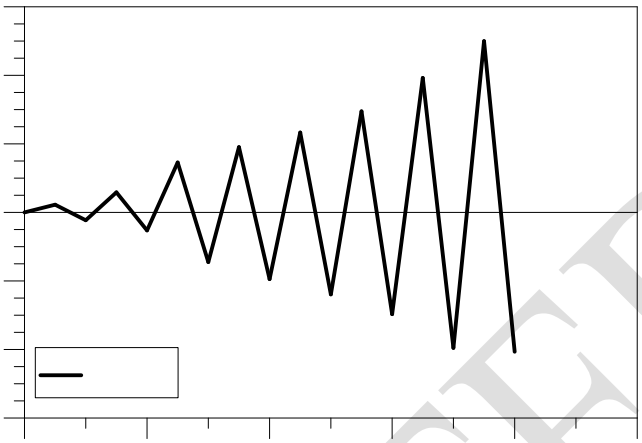

666

667 **Fig.5.** Horizontal displacement sequence for SC experiments (example for specimen MSR2).

668

669 # Figure 6

670

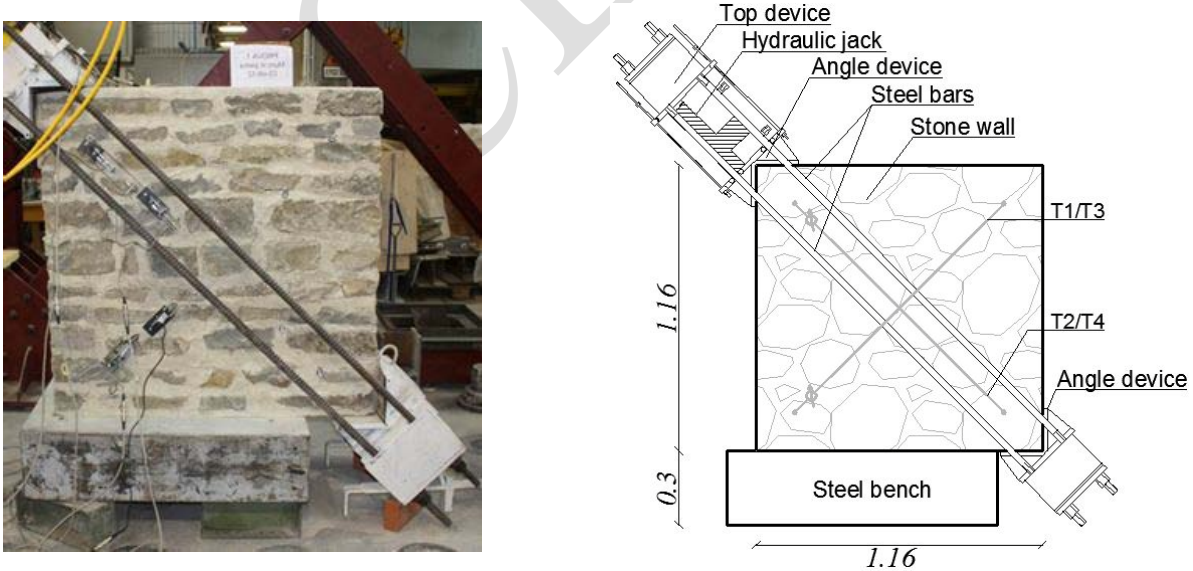

(a) (b)

Fig.6. DC experiments. (a) Test setup and (b) drawing of the experimental apparatus (nominal dimensions in m).

671

672

673

674 **Figure 7**

675

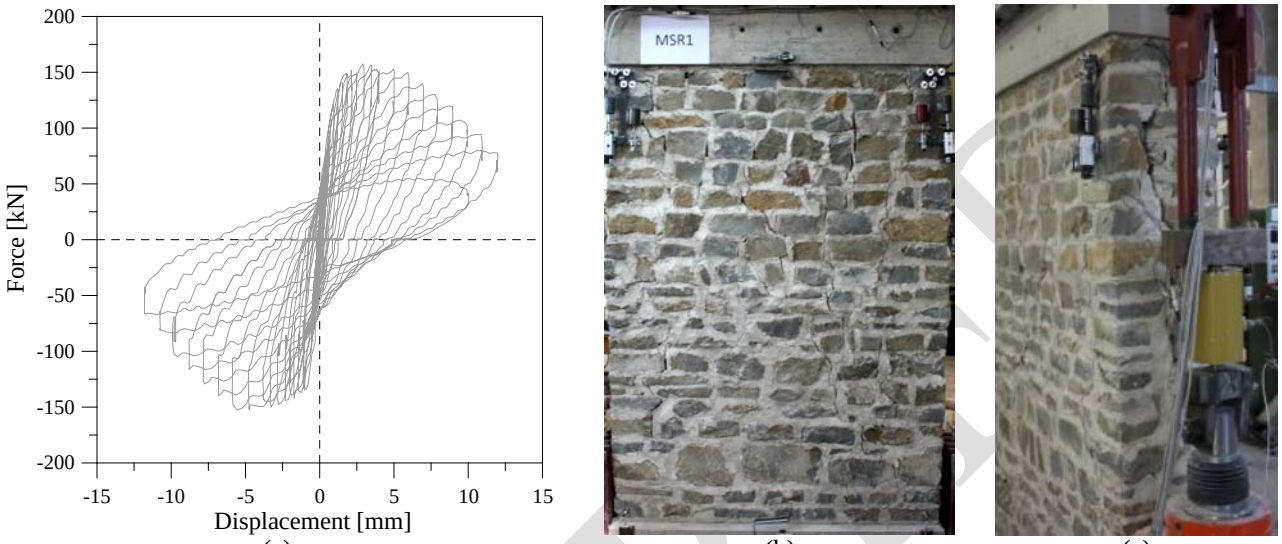

Fig.7. SC experiment of the URM specimen MSR1. (a) Load *H*-lateral displacement *u* cyclical behaviour; (b) crack pattern at the end of the test (front view); (c) failure configuration (detail).

676

677

678 **Figure 8**

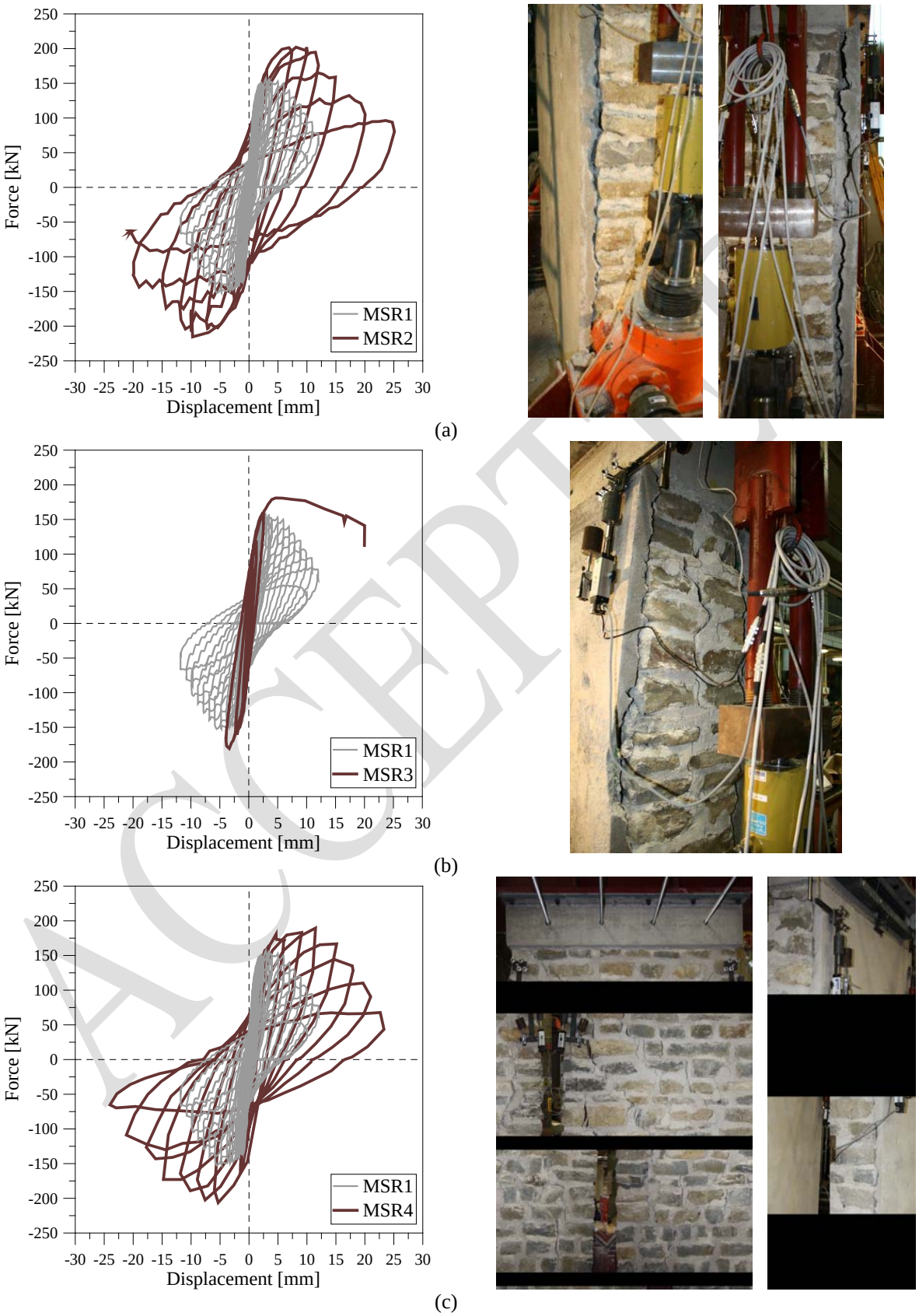

Fig.8. Load *H*-lateral top displacement *u* curves and failure configurations obtained from SC experiments. (a) Specimen MSR2; (b) specimen MSR3; (c) specimen MSR4.

679

680 **Figure 9**

681

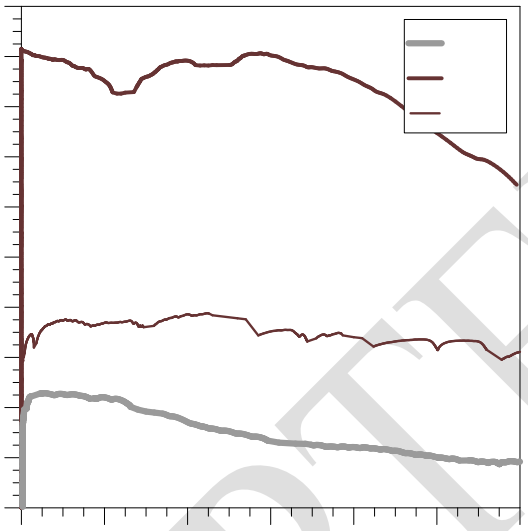

682

683 **Fig.9.** Load *C*-diagonal compression strain ε_c curves obtained from DC experiments (skeleton curves obtained from
684 cyclic test measurements). Positive strain ε_c denoting compressive shortening.
685

686 **Figure 10**

687

Fig.10. Diagonal crack in the URM specimen DC1.

688

689

690 **Figure 11**

691

Fig.11. Cracking of the reinforce coating in specimen DC2.

692

693

694 **Figure 12**

695

(a) (b) (c)

Fig.. DC experiment of the RM specimen DC3. (a) Crack pattern on the face treated with reinforced repointing; (b) evidence of out of plane deflection and (c) cracks in the face reinforced with the GFRP mesh.

696

697

698 **Figure 13**

699

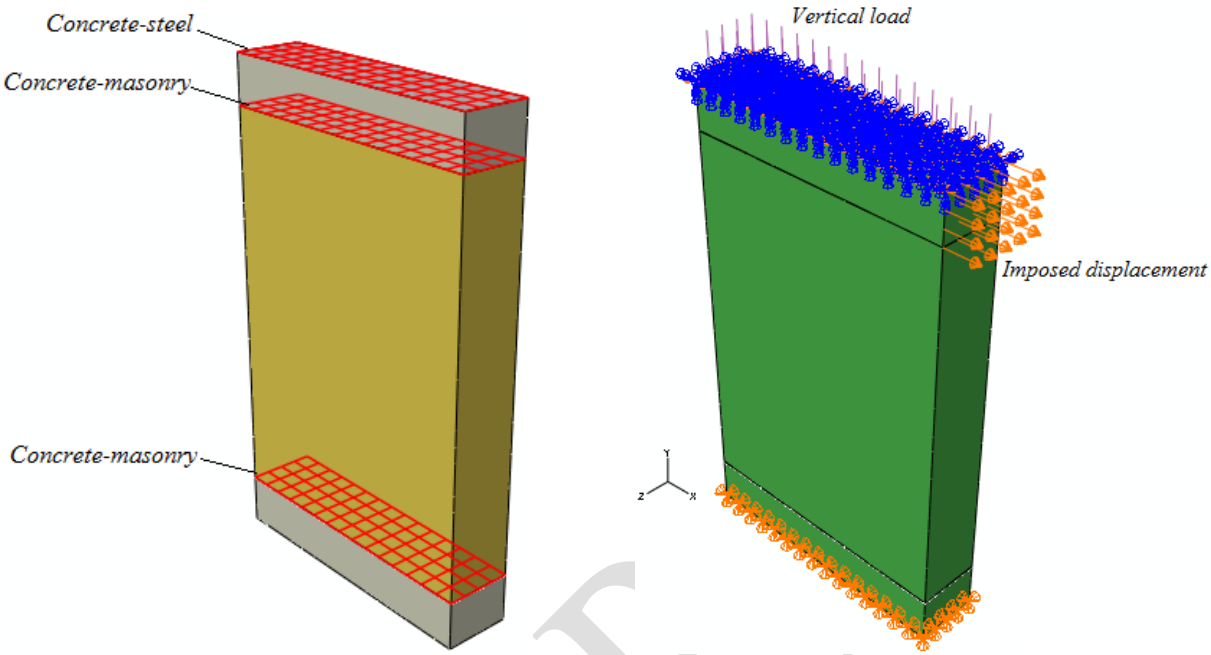

(a) (b)

Fig.13. FE-MSR1 numerical model (ABAQUS/Standard). (a) Concrete-masonry and concrete-steel contact surfaces for the introduction of "*tie*" constraints; (b) boundaries and loads.

700

701

702 **Figure 14**

703

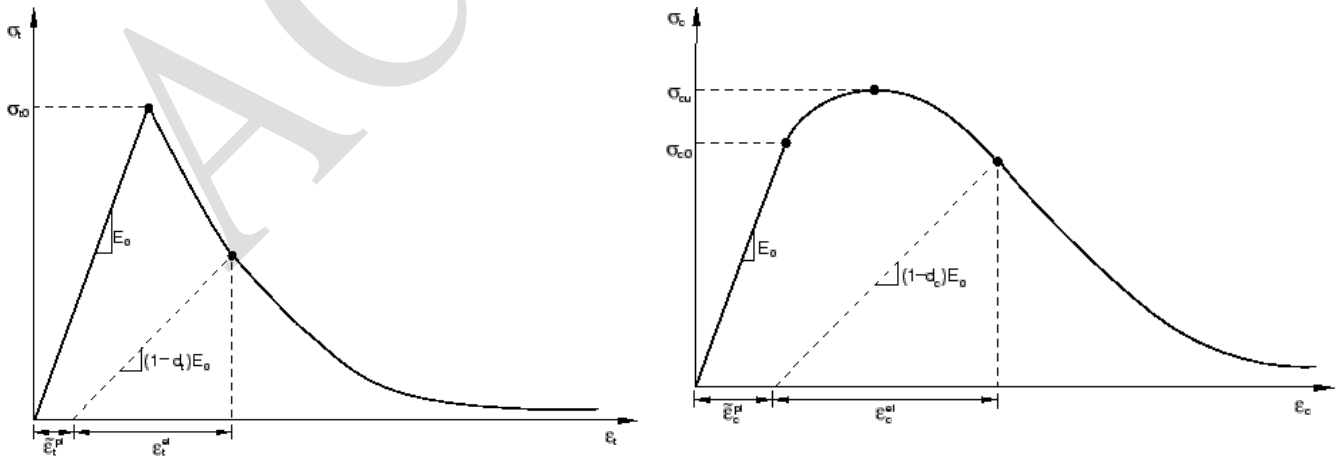

(a) (b)

Fig.14. Mechanical behaviour of masonry under uniaxial (a) tension and (b) compression [16].

704

705

706 **Figure 15**

707

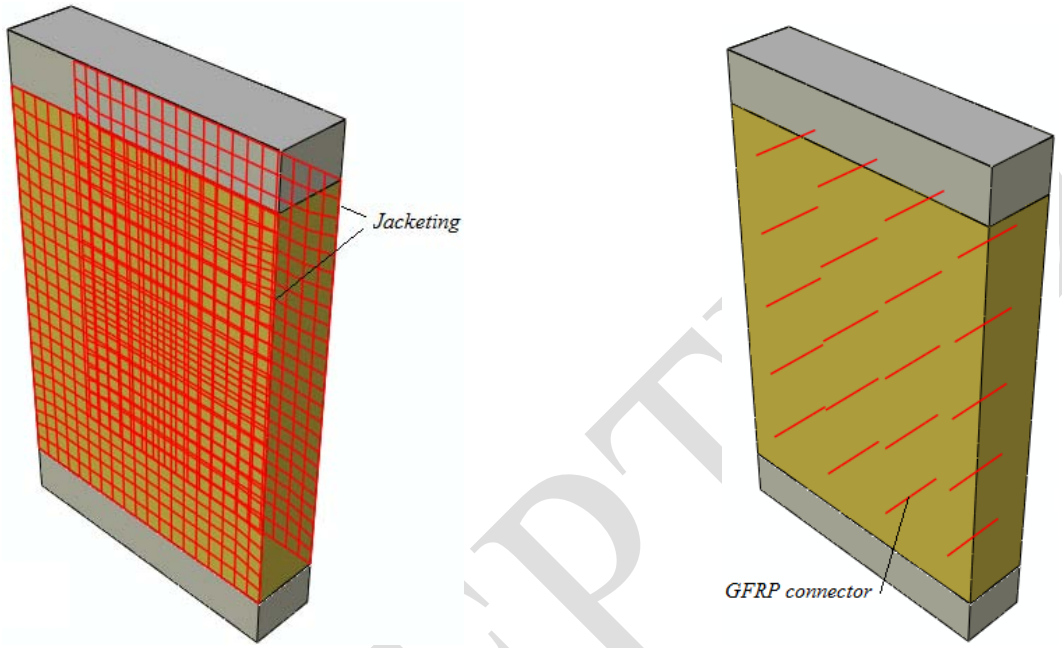

(a) (b)

Fig.15. FE-MSR2 numerical model (ABAQUS/Standard). (a) Contact surfaces at the interface between the masonry panel and the GFRM jacketing; (b) location of the GFRP L-shaped connectors.

708

709 **Figure 16**

710

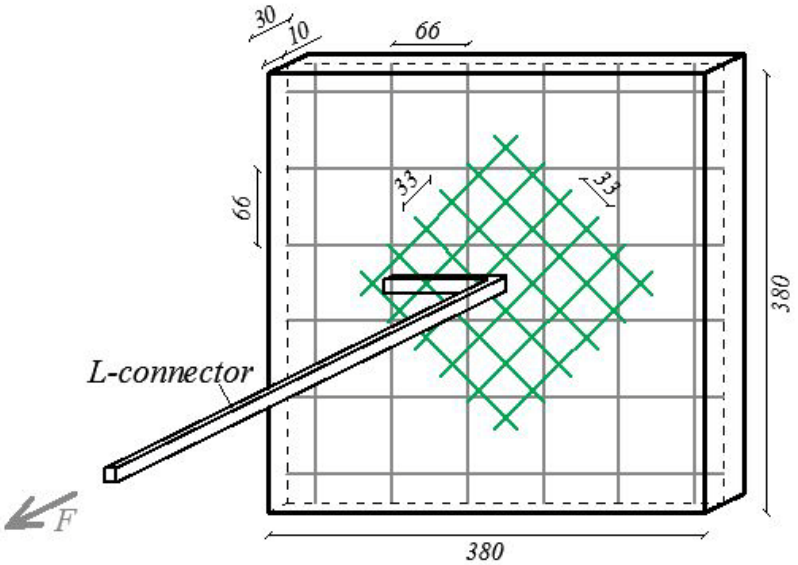

711

712 **Fig.16.** Test setup for the extraction experiments carried out on small specimens. Nominal dimensions in mm.

713

714 **Figure 17**

715

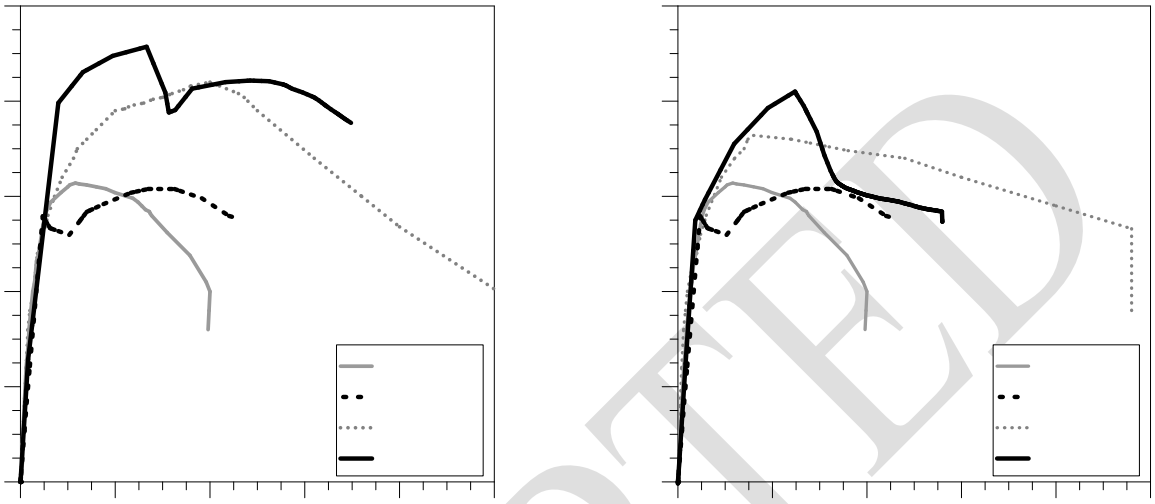

(a) (b)

Fig.17. Experimental (skeleton curve derived from cyclic test measurements) and numerical (ABAQUS/Standard) comparisons for the SC URM (MSR1) and RM specimens. (a) Specimen MSR2 (double GFRM jacketing); (b) specimen MSR3 (single GFRM jacketing).

716

717

718

719 **Figure 18**

720

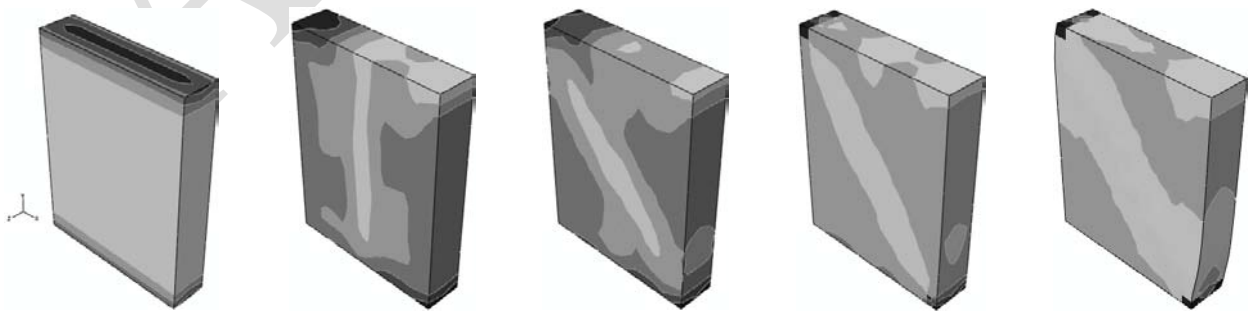

u_{max}= 0 u_{max}= 1mm u_{max}= 1.5mm u_{max}= 3mm u_{max}= 10mm

Fig.18. Qualitative distribution of maximum principal stresses in the URM specimen MSR1. Gray-scale contour plots tending from black (compression) to white (tension). ABAQUS/Standard.

721

722

723

724 **Figure 19**

725

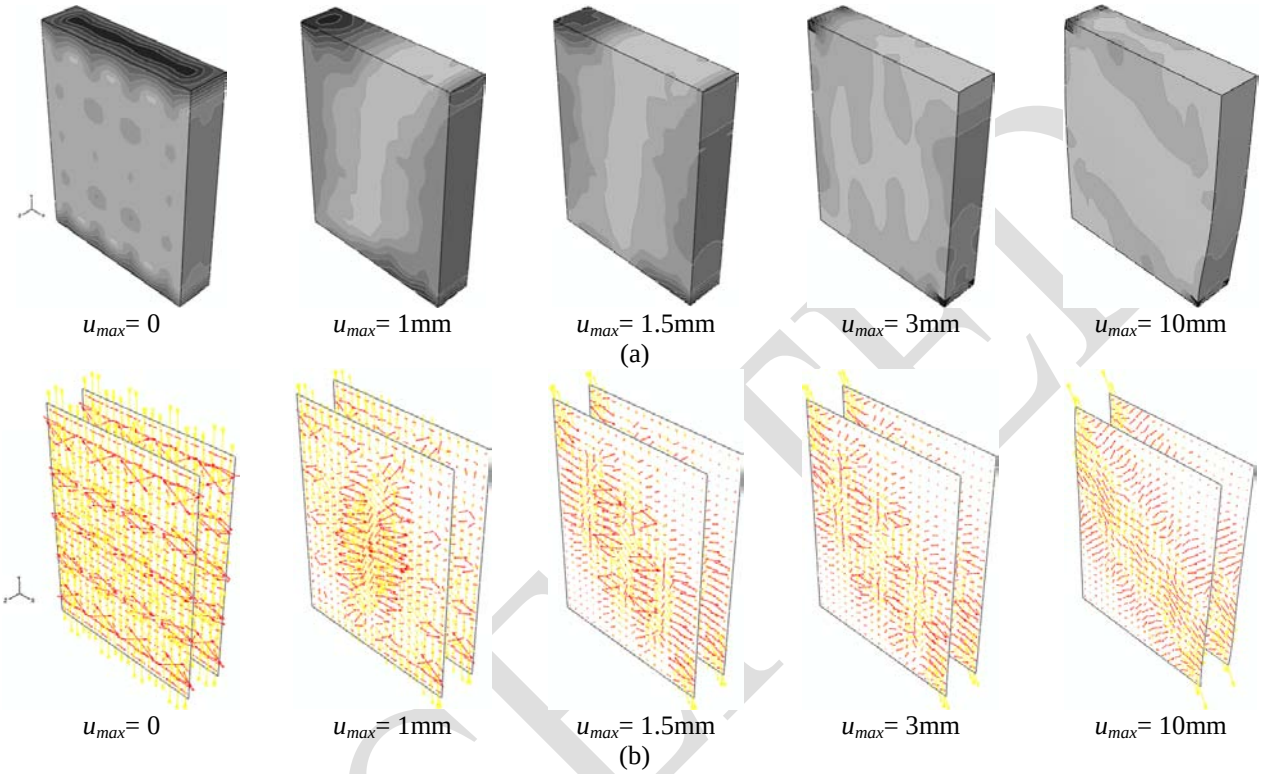

Fig.19. Qualitative distribution of maximum principal stresses in the RM specimen MSR2 (double GFRM jacketing). (a) Masonry panel; gray-scale contour plots tending from black (compression) to white (tension); (b) GFRM jacketing (vectorial representation). ABAQUS/Standard.

726

727

728 **Figure 20**

729

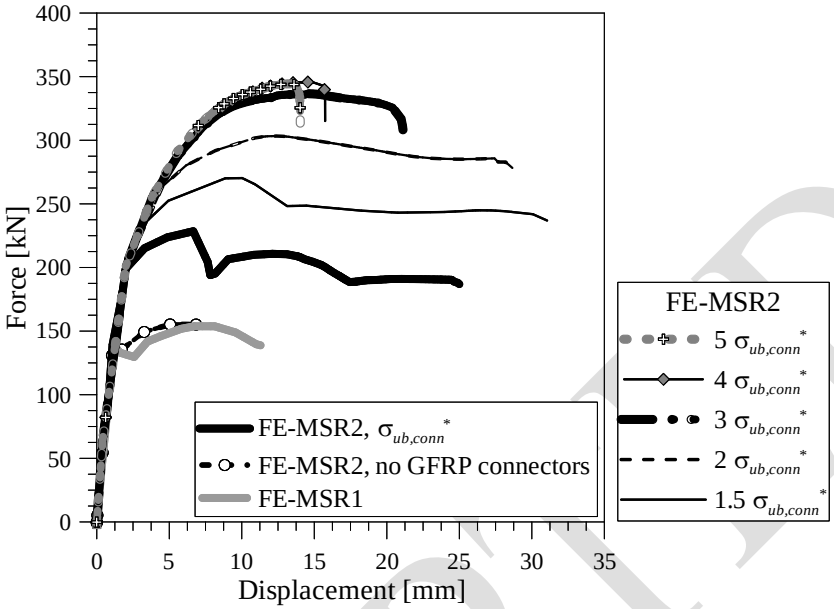

730
731 **Fig.20.** Strengthening effect of the L-shaped GFRP connectors (FE-MSR2), compared to the URM specimen
732 (FE-MSR1). ABAQUS/Standard.

733

734 **Figure 21**

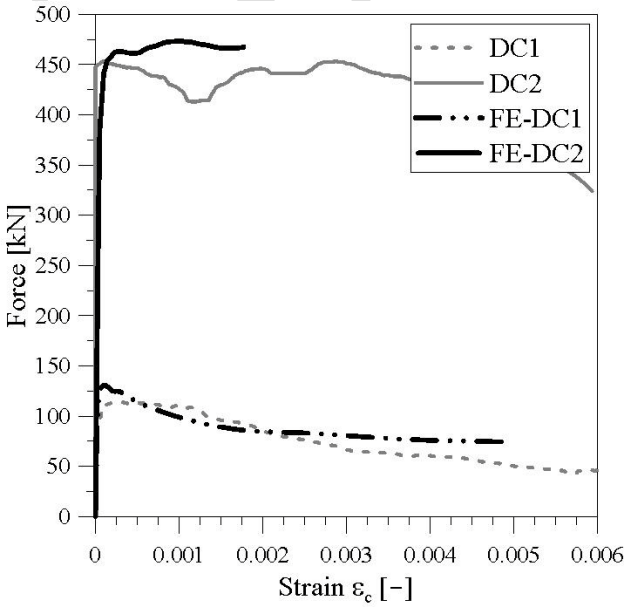

735
736 **Fig.21.** Experimental (skeleton curves derived from cyclic test measurements) and numerical (ABAQUS/Standard)
737 comparisons for the URM (DC1) and RM (DC2; double GFRM jacketing) specimens. Positive strain ε_c denoting
738 compressive shortening.
739

740

Table 1

Table 1. SC and DC experiments on URM and RM specimens.

Test	Specimen	Reinforcement	Reinforcement properties
SC	MSR1	-	-
	MSR2	GFRM jacketing	GFRP reinforced mortar coating on both the faces of the specimen
	MSR3	GFRM jacketing	GFRP reinforced mortar coating on a single face of the specimen
	MSR4	Hybrid technique	GFRP reinforced mortar coating on one face + "Reticolatus" on the other
DC	DC1	-	-
	DC2	GFRM jacketing	GFRP reinforced mortar coating on both the faces of the specimen
	DC3	Hybrid technique	GFRP reinforced mortar coating on one face + "Reticolatus" on the other

Table 2

Table 2. SC test results.

R_{load}= ratio between the maximum load H_{max} of RM specimens, compared to that of URM sample MSR1.

R_{disp}= ratio between the ultimate lateral displacement u_u of RM specimens, compared to that of URM sample MSR1.

R_t= ratio between the equivalent tensile strength f_t of RM specimens, compared to that of URM sample MSR1.

* Specimen subjected to a partial cyclic test protocol (Fig.8b).

Specimen	Maximum load H_{max}				Maximum lateral displacement u_{max}			Failure lateral displacement u_u			f_t [MPa]	R_t [-]
	Pos. [kN]	Neg. [kN]	Avg. [kN]	R_{load} [-]	Pos. [mm]	Neg. [mm]	Avg. [mm]	Avg. [mm]	u_u/h [-]	R_{disp} [-]		
MSR1	157	152	155	-	12.00	11.81	11.90	7.87	0.004	-	0.180	-
MSR2	209	222	216	1.39	25.15	20.38	22.77	14.98	0.007	1.90	0.312	1.73
MSR3*	182	181	181	1.17	24.14	3.96	14.05	20.05	0.010	2.55	0.234	1.30
MSR4	195	206	201	1.30	24.09	24.08	24.08	16.10	0.008	2.05	0.278	1.54

Table 3

Table 3. DC test results.
R_{load}= ratio between the maximum load C_{max} of RM specimens, compared to that of URM sample DC1.
R_{strain}= ratio between the shear strain γ_u at load 0.8 C_{max} and shear strain γ_{cr} at the onset of cracking.

Specimen	Maximum load C_{max} [kN]	R_{load} [-]	Shear strain γ_{cr} [-]	Shear strain γ_u [-]	R_{strain} [-]	Tensile strength f_t [MPa]
DC1	114	-	0.0019	0.0032	1.68	0.123
DC2	452	3.96	0.0044	0.0089	2.02	0.494
DC3	194	1.70	0.0035	0.0121	3.46	0.209

Table 4

Table 4. Input parameters for the mechanical characterization of masonry in the post-cracked regime (ABAQUS/Standard).

Tensile behaviour		Compressive behaviour	
f_t [MPa]	$\varepsilon_{pl,t}$ [-]	f_c [MPa]	$\varepsilon_{pl,c}$ [-]
0	0	0	0
0.1	0	2.5	0
0.1	0.0002	3.5	0.0035
0.03	0.0035		